
MISURE IS ALL YOU NEED TO EXPLAIN YOUR IMAGE SEGMENTATION

A PREPRINT

✉ **Syed Nouman Hasany**
Université de Rouen Normandie
syed-nouman.hasany@univ-rouen.fr

✉ **Fabrice Mériaudeau**
Université de Bourgogne
fabrice.meriaudeau@u-bourgogne.fr

✉ **Caroline Petitjean**
Université de Rouen Normandie
caroline.petitjean@univ-rouen.fr

June 21, 2024

ABSTRACT

The last decade of computer vision has been dominated by Deep Learning architectures, thanks to their unparalleled success. Their performance, however, often comes at the cost of explainability owing to their highly non-linear nature. Consequently, a parallel field of eXplainable Artificial Intelligence (XAI) has developed with the aim of generating insights regarding the decision making process of deep learning models. An important problem in XAI is that of the generation of saliency maps. These are regions in an input image which contributed most towards the model's final decision. Most work in this regard, however, has been focused on image classification, and image segmentation - despite being a ubiquitous task - has not received the same attention. In the present work, we propose MiSuRe (**M**inimally **S**ufficient **R**egion) as an algorithm to generate saliency maps for image segmentation. The goal of the saliency maps generated by MiSuRe is to get rid of irrelevant regions, and only highlight those regions in the input image which are crucial to the image segmentation decision. We perform our analysis on 3 datasets: Triangle (artificially constructed), COCO-2017 (natural images), and the Synapse multi-organ (medical images). Additionally, we identify a potential usecase of these post-hoc saliency maps in order to perform post-hoc reliability of the segmentation model.

Keywords XAI · explainability · image segmentation · saliency · CNN · transformer · sufficient region

1 Introduction

Following the success of AlexNet [Krizhevsky et al., 2012] in 2012 in the ImageNet competition, Deep Learning based algorithms - particularly CNNs and, more recently, transformers - swiftly dethroned the classical approaches in a variety of standard computer vision tasks. Multiple reasons have contributed to this success such as the availability of sufficient amounts of data as well as compute resources. Another such reason is the multi-layer, highly non-linear nature of these algorithms which allows them to model complex relationships given enough data. While this non-linearity affords high predictive performance, it also leads to the model not being inherently interpretable. Such models are often labelled as black-box models as opposed to the comparatively transparent white-box models (for example: decision trees) where the model is inherently interpretable allowing us useful insights as to why the model arrived at a particular decision. White-box models, however, are often too simplistic for computer vision problems, and fail to achieve reasonable performance criteria.

Naturally, a parallel field has since developed within Deep Learning which focuses on explaining model decisions. For the end-user, these explanations help improve their confidence in the model, whereas for a developer these explanations can help in a variety of ways such as identifying bias in the model. When it comes to explaining individual model

decisions (post-hoc local interpretability), two broad streams can be identified in deep learning: (i) **gradient** based, and (ii) **perturbation** based. Gradient based techniques [Simonyan et al., 2014, Smilkov et al., 2017, Sundararajan et al., 2017, Selvaraju et al., 2019] utilize the availability of the gradient associated with the model’s output with respect to the input image or to any of the intermediate activation maps. Perturbation based approaches [Zeiler and Fergus, 2014, Ribeiro et al., 2016, Lundberg and Lee, 2017, Petsiuk et al., 2018], on the other hand, rely on modifying the input image, and the corresponding change in the model’s output as a result of this modification. For a given model decision, both these streams output a saliency map indicating the region(s) in the input image which was supposedly the model’s focus.

Image classification has received the most attention when it comes to explainability approaches in deep learning based computer vision. Explainability approaches span a diverse set of tasks such as saliency maps, concept identification, counterfactual explanations, etc. Saliency maps are maps in which regions in an input image are highlighted in proportion to their contribution towards the final decision. Dense prediction tasks such as image segmentation have received far less spotlight in this regard. Some of the saliency generation approaches which have been developed for image segmentation are extensions of approaches proposed in the context of image classification where the only modification is made in terms of dealing with the model’s output - single valued prediction as opposed to a dense prediction - while the rest of the approach remains unchanged. A possible factor which has led to image segmentation receiving less attention is the relative lack of need for a saliency map when it comes to segmentation as opposed to classification. As the output of an image segmentation is a delineation of objects present in the input image, one can be led to the conclusion that the saliency in this case would simply be the individual objects themselves, hence rendering the need for an external process to generate explanations redundant [Dreyer et al., 2023].

Most of the methods proposed in the context of saliency generation in image segmentation are **gradient** based approaches. Specifically, they are extensions of Grad-CAM [Selvaraju et al., 2020] and its derivatives. A much smaller group belongs to the **perturbation** based approaches such as extension of RISE to image segmentation [Dardouillet et al., 2022]. Certain flaws can be identified in both these streams. When it comes to Grad-CAM in image classification, it is usually applied to the final feature extraction convolutional layer. This layer contains an effective summary of the image, and is solely responsible for the final model output. When it comes to extending Grad-CAM to image segmentation models such as U-Net, the choice of layer becomes non-trivial. Whereas the bottleneck can be thought of as the layer containing a summary of the image, it is hardly the only layer responsible for the final output decision. On the other hand, the layer responsible for the final output decision (just prior to the segmentation head) does not contain a summary of the original image. Even though most practitioners [Vinogradova et al., 2020] choose to generate the saliency map from the bottleneck layer, this choice is hard to justify. Additionally, CAM-based algorithms [Zhou et al., 2016] were designed for convolutional architectures and are not guaranteed to work for other architectures such as those involving transformers [Chen et al., 2021, Hatamizadeh et al., 2022]. Neither of these problems is encountered with perturbation based approaches as they are model agnostic. Perturbation based approaches such as RISE, however, tend to return a coarse saliency map which does not allow for the identification of precise locations of importance. The present work aims to solve both of these challenges.

In the present work, we propose a two stage method for generating saliency maps in image segmentation. In the first stage, motivated by the inductive bias inherent in the segmentation process, a mask is initialized focused on the object under consideration. This mask is gradually dilated until the segmentation model can successfully segment the object. The saliency map generated from this first stage represents a sufficient region which the model requires for a successful segmentation. In the second stage, taking inspiration from the work of Fong and Vedaldi [Fong and Vedaldi, 2017] in image classification, we optimize over the mask directly to prune this sufficient region in order to approximate a minimally sufficient region - where an ideal minimally sufficient region would only retain those portions of the input image without which the model will not be able to arrive at the correct segmentation. This approach ends up providing two saliency maps, where the sufficient region represents a coarser version of the explanation, and the minimally sufficient region represents a finer version. We also utilize our method to explore image segmentation in general in order to extract further insights with regards to the overall segmentation process. Finally, we explore the relationship between the generated saliency maps and the ground truth mask. This opens up the possibility for the post-hoc determination of reliable predictions from unreliable ones.

Our contributions can be listed as follows:

- We propose a model-agnostic two stage method for generating saliency maps in image segmentation, and showcase its application on three diverse datasets, one artificial (Triangle Dataset), one medical (Synapse multi-organ CT), and one natural (COCO-2017), both with convolutional and transformer based architectures ;
- We utilize our model to extract further insights with respect to the image segmentation process, regarding the size of the object to be segmented and the nature of the image (natural images vs. medical images);
- We identify a potential application of our saliency generation process as a proxy for post-hoc model reliability.

2 Related Work

2.1 Explainability in Image Classification

One of the earliest works in interpretability was of Zeiler and Fergus in 2013 [Zeiler and Fergus, 2014] in which they introduced a perturbation based technique, occlusion, as a means of generating a saliency map. Following that, a gradient based technique was proposed by Simonyan et al. [Simonyan et al., 2014] in which a saliency map was defined as the gradient of the output score with respect to the input image. This gradient based technique was further refined in subsequent works in which the primary focus was towards cleaning the otherwise noisy gradient information. Examples of such techniques include SmoothGrad [Smilkov et al., 2017] and IntegratedGradients [Sundararajan et al., 2017]. Instead of propagating the gradient all the way back to the input image, some techniques chose to rely on the intermediate activation space in order to generate a saliency map. Grad-CAM [Selvaraju et al., 2020] is one such approach in which a linear combination of activation maps from an intermediate network layer is considered as an explanation. The linear coefficients of this linear combination are obtained from the gradient of the output score with respect to the activation maps under consideration. Grad-CAM inspired many derivatives such as Grad-CAM++ [A. Chattopadhyay and Balasubramanian, 2018] and LayerCAM [Jiang et al., 2021]. Certain derivatives, however, identified the unreliability of using gradient information to compute the linear combination coefficients, and suggested alternate methods such as Score-CAM [Wang et al., 2020] and Ablation-CAM [Desai and Ramaswamy, 2020]. Where the original Grad-CAM utilized a single backward pass, these derivatives, however, required multiple passes, and coupled with the fact that they were not operating directly on the input image made them considerably less attractive compared to the original technique.

A number of perturbation based techniques have also been proposed which generally operate directly on the input image by modifying it, and observing the changes of the modification on the model’s output. Other than occlusion [Zeiler and Fergus, 2014], LIME [Ribeiro et al., 2016], SHAP [Lundberg and Lee, 2017], and RISE [Petsiuk et al., 2018] are popular techniques which generate multiple modified instances of the original image, and model the network’s behavior on these modifications using an inherently interpretable model. The generated modifications, however, are mostly random and do not take the network’s behavior on the input image under consideration. An alternate approach was proposed by Fong and Vedaldi [Fong and Vedaldi, 2017] which iteratively perturbs the input image guided by the gradient information - meaningful perturbations. The goal is to delete regions in an image which are maximally informative, and the removal of which would lead to the model changing its prediction. Alternatively, the goal can also be to end up with the minimally sufficient region of the input image which is necessary for the model to preserve the correct prediction.

2.2 Explainability in Image Segmentation

An early work which extended Grad-CAM to image segmentation was Seg-Grad-CAM by Vinogradova et al [Vinogradova et al., 2020]. Unlike image classification where there is a single output value, segmentation is a dense prediction task. In order to take this into account, a sum of scores from the region under consideration was taken as the output, the gradient of which was utilized to compute the linear coefficients. As the choice of network layer to generate a saliency map is not obvious in image segmentation¹, Mullan and Sonka proposed combining activation maps from each stage of the decoder instead of relying on a single layer [Mullan and Sonka, 2022]. Additionally, it was identified that Grad-CAM’s utilization of global average pooling to compute the linear coefficients might not work well when it comes to explaining a spatially local region in a segmented image [Wan et al., 2020, Hasany et al., 2023].

In terms of perturbation based techniques, occlusion [Gipiškis and Kurasova, 2023], SHAP [Dardouillet et al., 2022], and RISE [Dardouillet et al., 2022] have been extended to image segmentation whereby, for the latter two, a linear combination of the masks involved in generating the multiple modifications of the original input image serve as the explanation for the model’s output. Additionally, the meaningful perturbations approach was extended to image segmentation in which the input image is iteratively perturbed with the help of gradient information [Hoyer et al., 2019]. In this approach, however, perturbations are not applied to the segmented object to be explained leading to a contextual explanation.

While these methods are post-hoc locally interpretable methods, some work has also been done on global explainability in image segmentation. Janik proposed dimensionality reduction, and subsequent visualization of the bottleneck latent space as well as the identification of favorable and unfavorable regions for the model in this latent space [Janik et al., 2019]. Koker et al. proposed training a deep neural network for the sole purpose of predicting the saliency map guided by the original segmentation model which is frozen [Koker et al., 2021].

¹The original paper utilized the bottleneck layer of a U-Net model

Our work takes inspiration from both Fong and Vedaldi’s [Fong and Vedaldi, 2017] approach of meaningful perturbation as well as Hoyer et al.’s [Hoyer et al., 2019] extension of their approach to generate contextual explanations in image segmentation. Our departure from Hoyer et al.’s is primarily in three aspects. First, we explore the generation of a saliency map instead of a contextual explanation, and in doing so we allow perturbation to impact the object under consideration as well. This allows us to investigate whether the entirety of the object is, in fact, necessary for its successful segmentation. Second, we utilize the inductive bias inherent in the image segmentation process in order to initialize and refine our mask (using dilations) to arrive at a sufficient region before initializing the optimization based perturbation process. Third, our optimization goal is to maximize the Dice score between the model’s prediction on the perturbed image and its prediction on the original image as opposed to minimizing the l_1 norm between the two predictions.

2.3 Evaluation

A popular technique to evaluate saliency maps in image classification works by gradually adding portions of the image, starting with the most salient and ending with the least salient, such that by the end of the sweep the entire image content has been added. During this sweep the progression of the model’s output is tracked, and ideally, the model’s output should increase significantly as soon as the most salient regions of the image are added. This can be extended to image segmentation, and instead of the model’s output, one can utilize the Dice score between the prediction of the modified image and the prediction on the original image. However, Mullan and Sonka [Mullan and Sonka, 2022] recently proposed another technique specifically for image segmentation in which two scores are calculated, one corresponding to the segmentation performance on the input image masked by the saliency map - prediction preserved, and the second corresponding to the percentage of image pixels in the saliency map - image preserved. A saliency map preserving a smaller percentage of the image is better than one preserving a larger percentage given a similar segmentation performance.

3 Method

3.1 Generation of Sufficient Region (X_{SR}) and Minimally Sufficient Region (X_{MSR})

Let us consider a segmentation network f_θ parameterized by θ . Let us consider an image X_0 defined over a domain $\Omega \subset \mathbb{R}^2$ ($|\Omega| = N$ pixels) with values in \mathbb{R}^C where C is the number of channels, and its associated segmentation map Y_0 defined over domain Ω with values in $0, 1, \dots, L - 1$ where L is the number of classes.

Let l be the class for which a saliency map has to be generated. Let M be a mask of spatial dimensions $H \times W$ initialized as all ones. Given the inductive bias inherent in the image segmentation process, we initialize the mask with the assumption that the most salient region would encompass the segmented object itself. The mask is first resized to match the spatial dimensions of the image. Following that, we switch off our mask² on all spatial locations other than those corresponding to where the segmentation model predicted the class l for X_0 . This leads to an initial mask M_0 such that $M_0 = \mathbb{1}(Y_0)$ where $\mathbb{1}(\cdot)$ is the indicator function, equal to 1 when $Y_0 = l$ and 0 otherwise. Then the initialized mask M_0 is elementwise multiplied with the input image X_0 i.e. $X_m = X_0 \odot M_0$, where \odot refers to the Hadamard product. We use this X_m as the input to the segmentation model, and compute a Dice score between the model’s prediction on X_m denoted $f_\theta(X_m)$ and the model’s prediction on X_0 for the category l .

We define a threshold τ (0.9 in our case), and if the Dice score is above that, we consider M_0 to be the mask corresponding to a sufficient region. In case the Dice score (DSC) is less than the threshold, we dilate our mask, and repeat the process until the Dice score is above the threshold. The mask M_{SR} obtained from this process is elementwise multiplied with the input image in order to generate the region that we refer to as the "sufficient region" (SR) i.e. $X_{SR} = X_0 \cdot M_{SR}$.³ This method is summarized in algorithm 1.

In the second step, our goal is to refine X_{SR} in order to find the minimally sufficient region X_{MSR} . In order to achieve this, we define the following optimization objective:

²switch off implies zeroing the values

³in a case where M_0 requires zero dilations, M_0 is identical to M_{SR}

Algorithm 1 Finding M_{SR}

```

1: function FINDING  $M_{SR}$  :
    $M_{SR} = M_0$ 
2: while  $DSC(f_\theta(X_0), f_\theta(X_m)) \leq \tau$  do
3:    $M_0 \leftarrow dilate(M_0)$ 
4:    $X_m \leftarrow X_0 \odot M_0$ 
5: end while
6: return  $X_{SR} = X_m, M_{SR} = M_0$ 
7: end function

```

$$\begin{aligned}
M_{MSR} = \arg \min_{M_{SR}} & \frac{\lambda}{|\Omega|} \sum_{u \in \Omega} \|M_{SR}(u)\|_1 + \gamma \sum_{u \in \Omega} \|\nabla M_{SR}(u)\|_\beta^\beta \\
& + \left\{ 1 - \sum_{i \in \{0, l\}} \alpha_i \frac{\sum_j^N 2f_\theta(X_{SR} \odot M_{SR})_i^j f_\theta(X_0)_i^j + \epsilon}{\sum_j^N f_\theta(X_{SR} \odot M_{SR})_i^j + \sum_j^N f_\theta(X_0)_i^j + \epsilon} \right\}
\end{aligned} \tag{1}$$

The first term with λ as its hyperparameter is the absolute average of the M_{SR} , the goal of the optimization is to decrease this as much as possible with the aim of removing unnecessary regions from the mask. The second term with γ as its hyperparameter is the total variation (TV) regularization which contributes towards the mask being smooth. Following that we have the Dice loss. The goal is to minimize the Dice loss in category l between the prediction on the original image and the prediction on the perturbed image where the perturbation is defined as $\phi_{SR} = X_{SR} \odot M_{SR}$.⁴ The preservation terms for the foreground and background Dice can potentially have different coefficients with $\alpha_l \geq \alpha_0$ in order to favor the preservation of the foreground. j is the index over the total number of pixels (N) in a channel. The output from this step (eq. 1) M_{MSR} is utilized to generate our minimally sufficient region X_{MSR} :

$$X_{MSR} = X_{SR} \odot M_{MSR} \tag{2}$$

Even though X_{SR} is generated to provide a better initialization for the optimization step, it can, in itself, be seen as an explanation alongside X_{MSR} with the former providing a coarser explanation, and the latter providing a much finer one.

3.2 Extracting Global Insights on the Segmentation Process

By design, the saliency maps we generate belong to the genre of local explainability techniques in which a method is applied to explain decisions for individual data instances. Features from individual saliency maps can, however, be combined allowing for further analysis. We plot (i) the number of dilations required for X_{SR} vs. the prediction size as well as the (ii) the evaluation metric vs. the prediction size. These two plots allow us to observe a general trend in the overall segmentation process.

3.3 Post-Hoc Assessment of the Segmentation Model Reliability

The purpose of saliency maps is usually to either increase the confidence of the end user in the model’s predictions or to help the developer debug the model in order to improve its performance. In the present work, we explore the relationship of saliency maps to the post-hoc reliability of the segmentation model. Given the assumption that saliency maps for incorrect model predictions are potentially different from those of saliency maps for correct model predictions, we experiment with training a discriminator which can allow us to identify whether our model is correct in its prediction or whether it has faltered. The features utilized to train this discriminator model are extracted from the saliency maps themselves. The utility for such a discriminator is evident as it can allow us to automatically judge the model’s predictions for cases where the ground truth labels are not available.

3.4 Evaluation

Given the inherently subjective nature of explainability, there is a lack of consensus when it comes to metrics involving saliency maps. Occasionally, works limit themselves to a qualitative analysis based on the visual results of the saliency

⁴It is indeed possible to replace Dice with other losses such as the cross entropy loss

maps. In the present work we present both a qualitative as well as a quantitative analysis based on metrics which shall briefly be discussed below.

For a quantitative metric we take inspiration from Mullan and Sonka [Mullan and Sonka, 2022]. They proposed two metrics which jointly take both the segmentation performance as well as the image preservation into account when evaluating saliency maps. For the first of these metrics, a Dice score is calculated between the model’s prediction on X_{MSR} , and the model’s prediction on the original image in order to determine how well the region relevant to the prediction was captured by the saliency map. We refer to this as **Dice explained**. For the second metric, the percentage of non-zero pixels in the saliency map is computed in order to quantify the size of the image which was preserved. We modify this latter percentage, and instead calculate the ratio of the sum of non-zero pixels in the saliency map to the number of pixels in the segmented object. We refer to this as the **perturbation ratio**. A good saliency generation method is going to have a high Dice explained (as close to 1 as possible) and a low perturbation ratio.

4 Experiments

4.1 Datasets and Models

We conduct our experiments on three diverse datasets, one of them being artificially generated, one being medical in nature, and the last consisting of natural images. The artificially generated dataset is inspired from Riva et al. [Riva et al., 2022]. This dataset, called Triangle, is generated by placing objects from the Fashion-MNIST on a blank image. Three objects are placed in a triangular fashion such that the objects’ centers form the vertices of a triangle. The other objects are randomly placed. The goal of a model is to only segment those objects which are part of the triangle, and consider the randomly placed objects as being part of the background (see Fig. 1 for examples). We generate 2000 samples, 1400 of which are for training, and the remaining 600 for validation. We trained a U-Net (VGG-16 backbone) on this dataset for our saliency experimentation.

The second dataset is the Synapse multi-organ CT dataset [Landman et al., 2015] consisting of 30 abdominal CT scans, 18 of which are used for training and 12 for validation. In total we have 2211 2D slices for training, and 1568 slices for validation. The labels are: Aorta, Gallbladder, Left Kidney, Right Kidney, Liver, Spleen, Pancreas, and Stomach. We trained a U-Net (ResNet-34 backbone) [Ronneberger et al., 2015] as well as a TransUNet [Chen et al., 2021] on this dataset for our saliency experimentation.

The final dataset is the COCO-2017 dataset [Lin et al., 2014] from which we select the following labels: Bus, Car, Cat, Cow, Dog, Bike, Person, and Train. For our saliency experimentation we utilized a pre-trained DeepLabV3 (ResNet-50 backbone) [Chen et al., 2017] model.

4.2 Experimental Configuration

For the saliency experiments, we use a single channel mask with a size of 224×224 (for mask initialization, images are accordingly resized to these dimensions). The AdamW optimizer is utilized with a learning rate of 0.1 and the coefficient for the absolute average loss λ (eq. 1) is 0.01. Following Hoyer et al. [Hoyer et al., 2019], after every iteration of the optimization process, any value of the mask less than 0.2 is clamped to 0, and any value above 1 is clipped to 1. We perform the optimization for 100 iterations. In order to generate the M_{SR} , we use a circular dilation kernel of size 7×7 . We use a coefficient of $\alpha_0 = 1$ for the background Dice and a coefficient of $\alpha_l = 2$ for the foreground Dice. We also present results for alternate parameter combinations in order to contextualize our parameter choices.

4.3 Evaluation

For a qualitative analysis, sample saliency maps are shown. For a quantitative analysis, our primary evaluation metrics are the **Dice explained** and the **perturbation ratio**. We report the mean performance of our saliency method for both these metrics on a subset of our utilized datasets.

4.4 Comparison to Baselines

We compare our saliency method against the most popular saliency generation method in image segmentation, Seg-Grad-CAM [Vinogradova et al., 2020], a gradient based method. We also compare it to a perturbation based method, RISE [Dardouillet et al., 2022], as it is also a model-agnostic saliency generation method. RISE works on a perturbation based scheme whereby randomly generated masks are applied to the input image; and for each of those masked images, a Dice score is calculated between the prediction on the masked image and the prediction on the original image. A

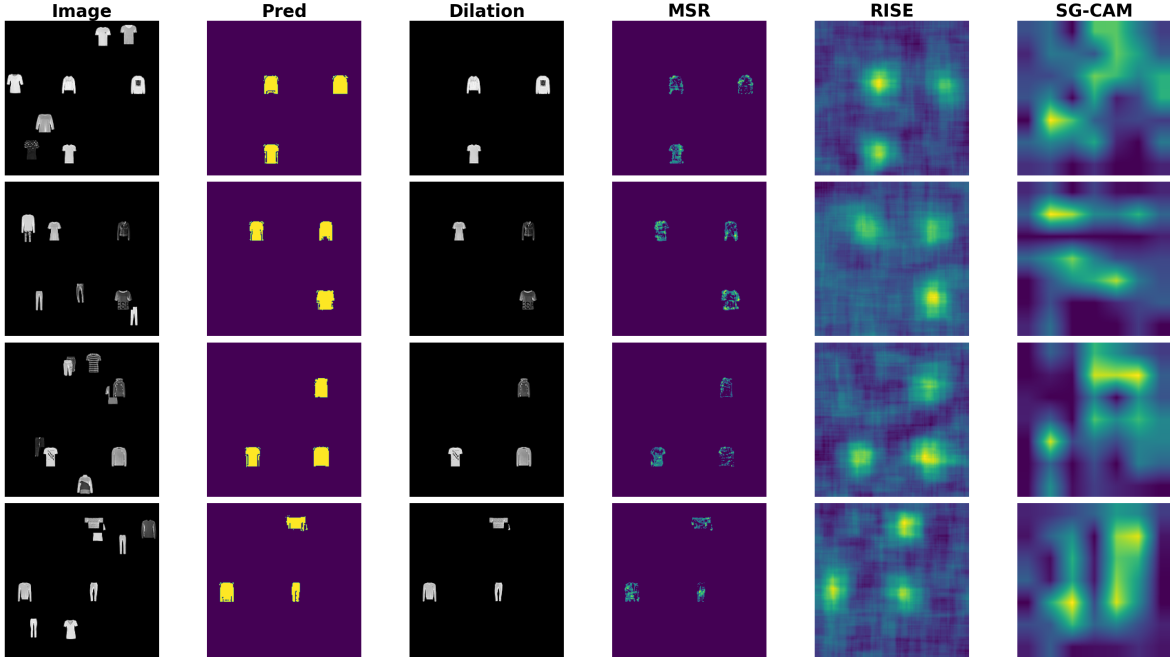


Figure 1: Sample results (in row) from the Triangle dataset. The column 'Dilation' refers to X_{SR} whereas column 'MSR' (saliency map) refers to M_{MSR} . SG-CAM: Seg-Grad-CAM. Results are best viewed zoomed-in.

linear combination of the generated masks serves as our explanation where the coefficients are the aforementioned Dice scores. For our experiments we use Seg-Grad-CAM on the bottleneck layer, and RISE with 2000 masks.

We compare both qualitatively (based on the visual saliency map) as well as quantitatively using the Dice explained and perturbation ratio metrics. Saliency maps from both RISE and Seg-Grad-CAM are first thresholded followed by an elementwise-multiplication of the binarized saliency map with the original image. For Seg-Grad-CAM, thresholds of 0.05 and 0.1 are experimented with, whereas for RISE, thresholds of 0.2 and 0.4 are utilized.

5 Results and Discussion

5.1 Sample Saliency Maps

Figure 1 shows saliency maps generated for a few samples of the Triangle dataset. In all cases, it is apparent that the saliency map generated by MSR and RISE broadly agree in their localization. Seg-Grad-CAM, on the other hand, has generated significantly divergent saliency maps. Between MSR and RISE, the main difference lies in the map's fineness. MSR's maps are considerably finer in which the most prominent regions appear to be the boundaries of the objects. For RISE, however, saliency maps are fairly coarse, and despite them being most active for the three objects, they fail to disclose any further information with regards to delineating the exact region important for the segmentation model.

Figure 2 shows saliency maps generated for a few samples on the Synapse dataset. Once again, we see agreement in localization between MSR and RISE, independently from the model (U-Net vs. TransUNet), with the primary difference in saliency maps being that of fine vs. coarse. In the case of MSR, a comparison of the **Dilation** column to the **MSR** column also allows us to see the importance of optimization following the dilation step as it leads to non-essential information being pruned away. For Seg-Grad-CAM, there is a big discrepancy, depending on the model: where saliency maps obtained on UNet may show some localization correspondence with RISE, those obtained on TransUNet are highly questionable, and highlight the inadequacy of Seg-Grad-CAM for non-convolutional architectures.

Figure 3 shows saliency maps generated for a few samples on the COCO-2017 dataset. In this case, all three methods seem to broadly agree on localization. From a spectrum of coarse to fine, RISE returns the coarsest saliency maps, and MSR returns the finest, with Seg-Grad-CAM being in between. Some interesting samples are from rows five, six, and seven where results from MSR and Seg-Grad-CAM not only agree on the overall localization, but also on the general

shape. Row seven is particularly interesting as both MSR and Seg-Grad-CAM only highlight the boundaries of the object (train) while ignoring the remaining portion of the object almost entirely.

Focusing on the MSR, we observe that for both the Triangle dataset as well as the COCO-2017 dataset, the saliency maps tend to indicate that the segmentation models are highly influenced by the objects' boundaries whereas for the Synapse dataset, the object itself appears to be more important for the segmentation model. For our particular case it appears that segmentation models rely on different features when it comes to segmenting natural images as compared to medical images. In the case of natural images, the contours appear as the most important feature whereas for medical images, it is the entire object itself instead of its mere boundary. While this observation requires further experiments in order to arrive at a general conclusion, medical and natural images being of a different nature in terms of their intrinsic dimensions [Konz et al., 2022] might explain this difference in the segmentation models' behavior.

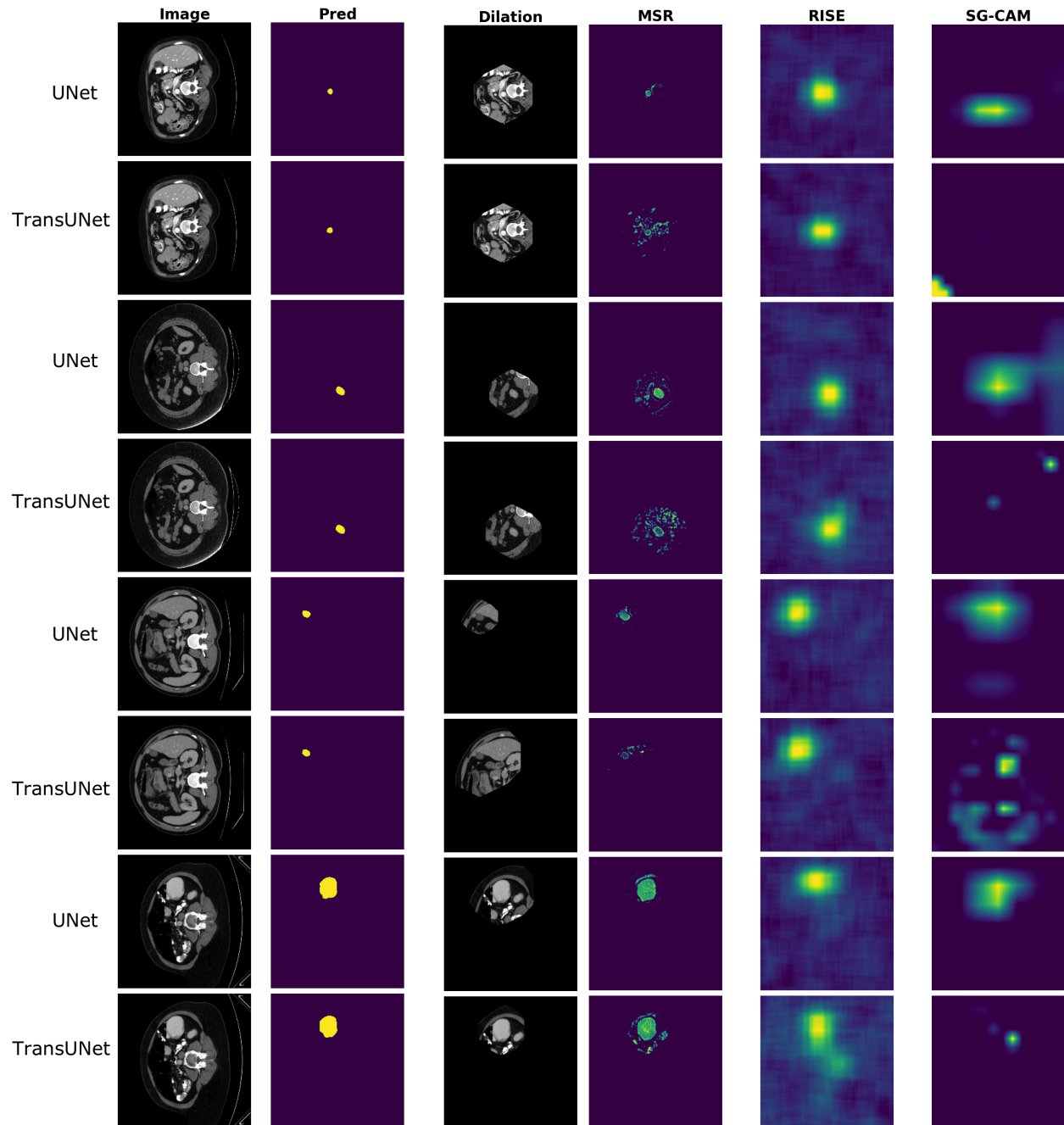


Figure 2: Sample results from the Synapse multi-organ CT dataset, from U-Net and TransUNet. Each pair of rows (top-to-bottom) represents a class to be explained: Aorta, Left Kidney, Gall Bladder and Liver. Dilation refers to X_{SR} whereas MSR (saliency map) refers to M_{MSR} . Results are best viewed zoomed-in.

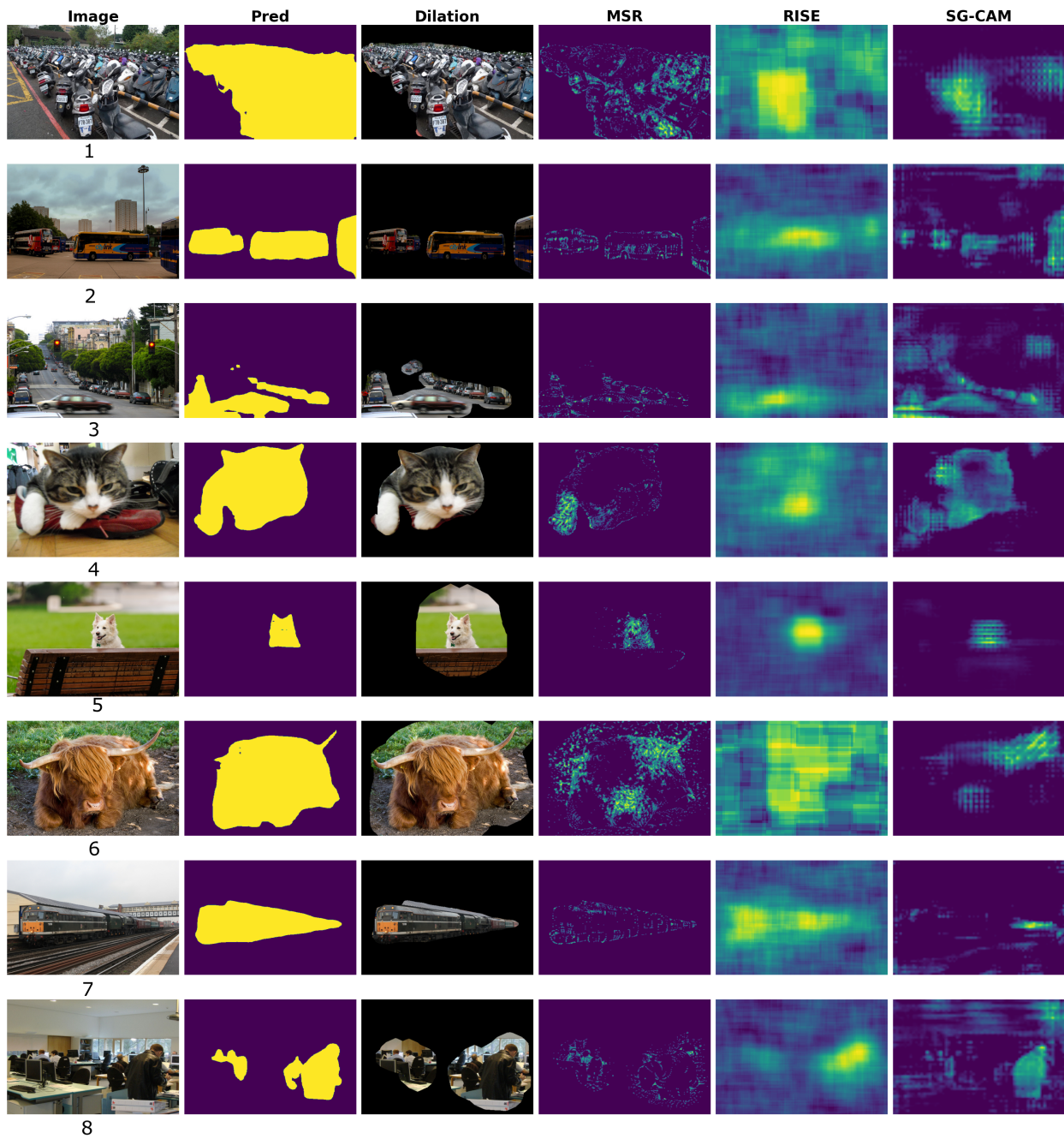


Figure 3: Sample results from the COCO-2017 dataset. Row number is below the image. Each row (top-to-bottom) represents a class to be explained: Bike, Bus, Car, Cat, Dog, Cow, Train and Person. Dilation refers to X_{SR} whereas MSR (saliency map) refers to M_{MSR} . Results are best viewed zoomed-in.

5.2 Dice Explained and Perturbation Ratio

Table 1 records the results on a subset of the Triangle, Synapse, and COCO-2017 datasets. In terms of Dice explained, RISE (with a binary threshold of 0.2) consistently outperforms the other methods with MSR following it. Whereas when it comes to perturbation ratio, MSR is the clear winner. It can also be observed that the perturbation ratios of MSR are less than the others by an order of magnitude.

Interestingly, for both the Triangle as well as the COCO-2017 datasets, the perturbation ratios obtained from MSR are less than 1. This means that the necessary region required by the segmentation model in order to segment an object contained *fewer* pixels than the object itself - two-thirds in the case of Triangle and one-fifth in the case of COCO-2017. The perturbation ratio obtained from MSR for Synapse, on the other hand, is more than 1. For the Triangle dataset, it can be surmised that the objects and the backgrounds are simple enough such that the model can segment the entire object merely by identifying the outline. For Synapse, given that the objects to be segmented are often similar in texture to their surroundings, the required context is naturally greater. These hypothesis, however, require further investigation.

Compared to RISE and MSR, Seg-Grad-CAM does not obtain good results. The only dataset for which Seg-Grad-CAM performs comparatively well is the COCO-2017 dataset. This corroborates well with the visual results presented in Section 5.1 (Figure 3). We also observe that in Synapse’s case, Seg-Grad-CAM’s application on TransUNet is worse than Seg-Grad-CAM’s application on U-Net. This reinforces the notion that caution should be exercise while importing Grad-CAM based algorithms to transformer based architectures.

In terms of computational performance, Seg-Grad-CAM is the quickest taking less than a second whereas RISE is the slowest taking around a minute. MSR takes around 3 to 4 seconds to process a single image. However, given the other two performance metrics, it is clear that Seg-Grad-CAM can hardly be the ideal contender for generating saliency maps in image segmentation. If all metrics are taken into account, MSR emerges as the most balanced of the three algorithms.

Finally, it is worth noting that the thresholds have a considerable impact on both RISE and Seg-Grad-CAM. With a smaller threshold, more pixels from the input image are included. Naturally, this leads to a better Dice explained at the expense of a worse perturbation ratio. MSR requires no threshold as its values are determined directly by the optimizer.

5.3 Investigating the influence of the object size on the segmentation model

We further investigate the utility of saliency maps in terms of providing us with insights regarding the global process of segmentation, with respect to the size of the object to be segmented. We explore (i) the **number of dilations** required in order to arrive at the X_{SR} , and (ii) the **perturbation ratio**. Both of these are plotted against the prediction size. Figures. 4 and 5 display these plots for the Synapse dataset for the U-Net and TransUNet respectively. Figures. 6 and 7 displays them for the Triangle dataset and COCO-2017 dataset respectively.

In general, we observe a decreasing trend for both the number of dilations as well as the perturbation ratio as the object’s size increases for both the Synapse as well as COCO-2017 datasets. Additionally, we observe this trend for all three of our models: U-Net, DeepLabv3, and TransUNet. For a smaller prediction size, the perturbation ratio and the number of dilations are higher as opposed to a larger prediction size. This implies that the model seems to be requiring comparatively more visual data in order to segment smaller objects whereas as the size of the objects increase, the relative requirement of visual data decreases. In other words, the size of the object to be segmented and the relative amount of visual data required by the segmentation model to successfully segment it follows a roughly inverse relationship.

The absence of this trend in the Triangle dataset can be attributed to its artificial nature. Given the similarity of objects to be segmented as opposed to the inherent diversity present in the medical and natural images datasets, the perturbation ratio as well as the number of dilations remained fairly constant across different input samples.

5.4 Impact of Parameters

We utilized a learning rate of 0.1 for the optimizer to find the MSR, a λ of 0.01, and a mask size of 224×224 for our experiments. In the following two sections we report results for a variety of other parameter configurations in order to justify our choice.

5.4.1 Learning rate vs. λ

We report results for 9 pairs of learning rate and λ such that each parameter takes on a value of 0.001, 0.01, and 0.1. Results for the Triangle dataset are displayed in Table. 2, results for the Synapse dataset are displayed in Tables 3 and 4 for U-Net and TransUNet respectively, and results for the COCO-2017 dataset are displayed in Table 5. It is

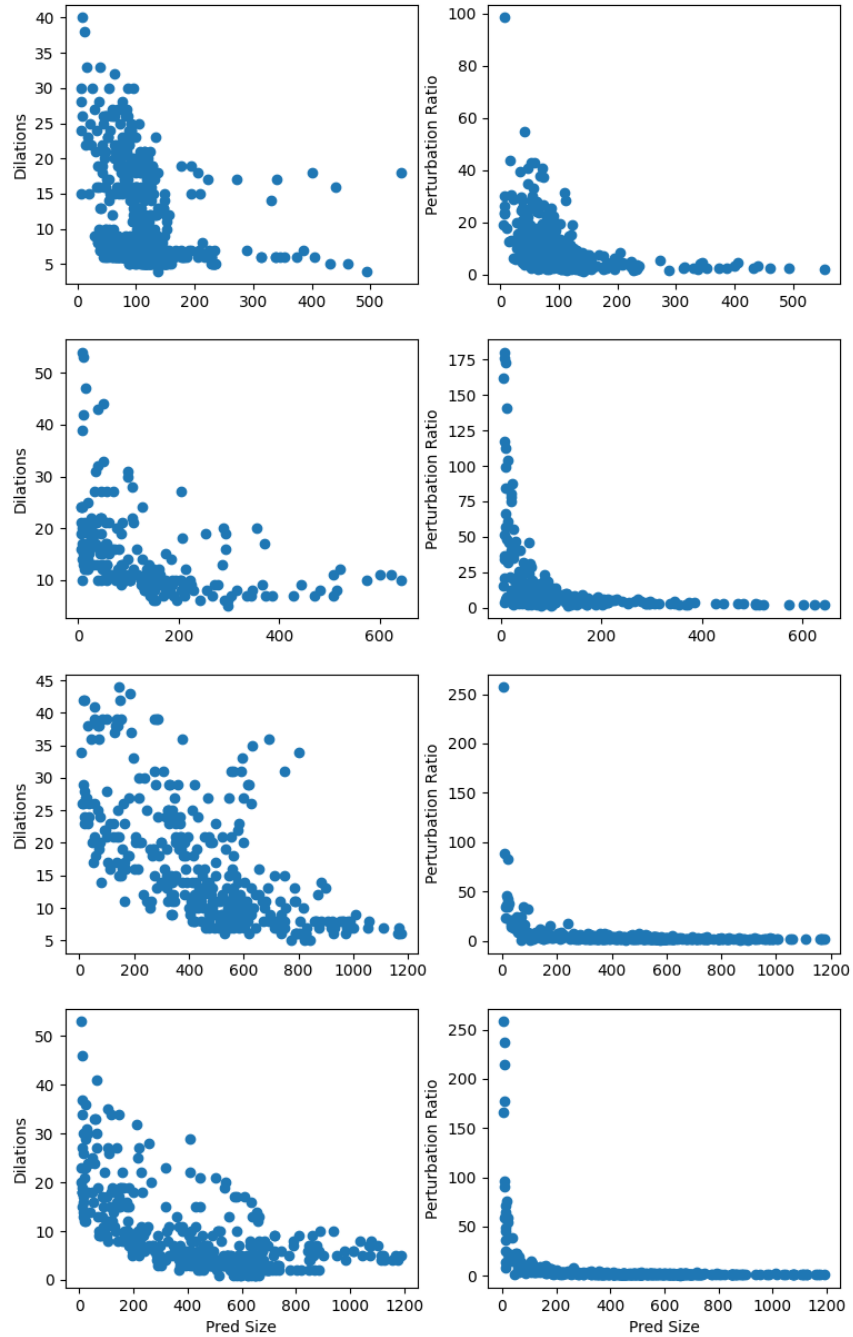


Figure 4: Impact of Prediction Size on the Synapse multi-organ CT dataset for U-Net. Plots of the No. of Dilations against the Prediction size (left), and the Perturbation Ratio against the Prediction size (right). The plots, from top-to-bottom, are for the categories: Aorta, Gall Bladder, Left Kidney, Right Kidney.

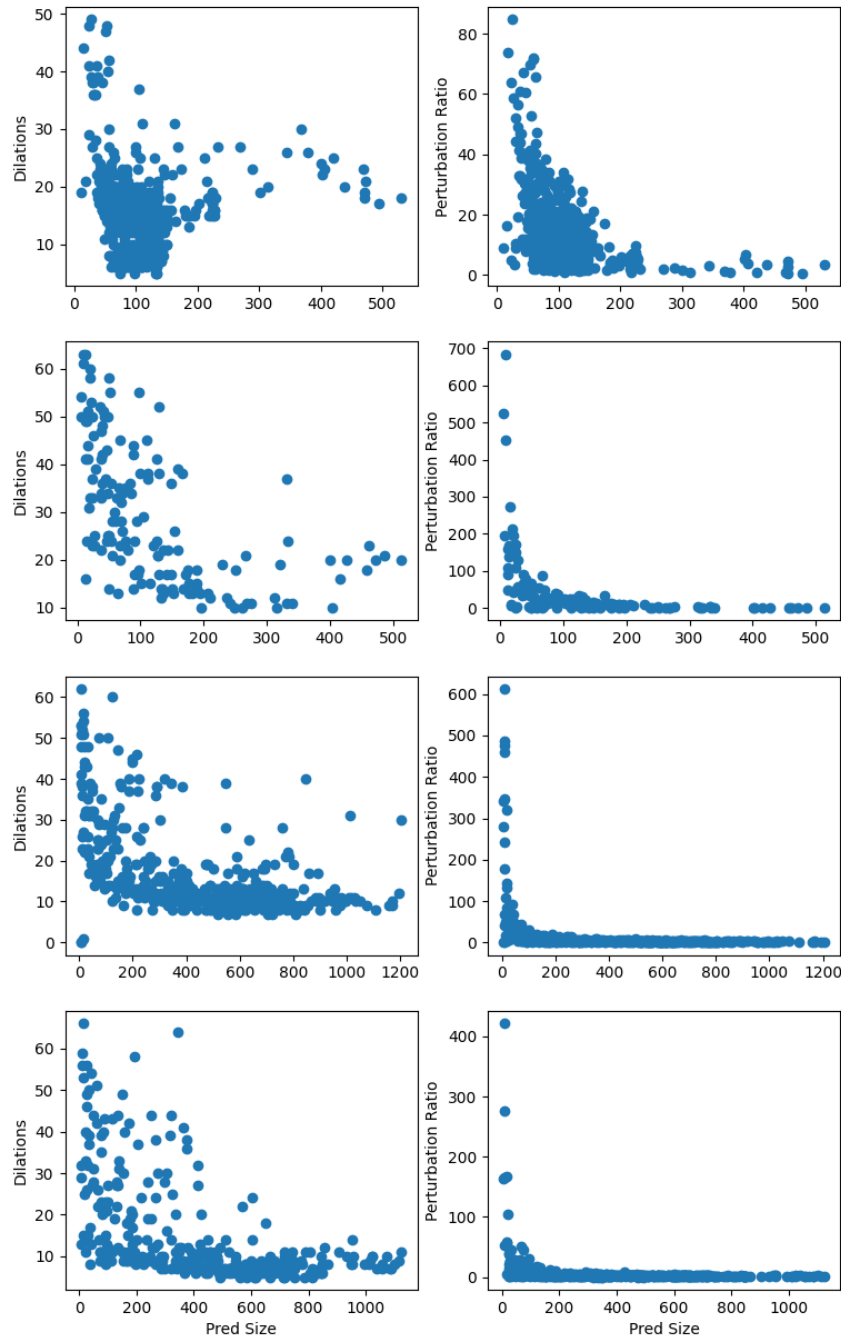


Figure 5: Impact of Prediction Size on the Synapse multi-organ CT dataset for TransUNet. Plots of the No. of Dilations against the Prediction size (left), and the Perturbation Ratio against the Prediction size (right). The plots, from top-to-bottom, are for the categories: Aorta, Gall Bladder, Left Kidney, Right Kidney.

Dataset	Model	XAI Method	Binary Threshold	Dice Explained	Perturbation Ratio	Time (s)
Triangle	U-Net	Seg-Grad-CAM	0.05	0.665	27.38	0.067
Triangle	U-Net	Seg-Grad-CAM	0.1	0.553	16.86	0.067
Triangle	U-Net	RISE	0.2	0.995	26.07	52
Triangle	U-Net	RISE	0.4	0.984	5.83	52
Triangle	U-Net	MSR	-	0.965	0.63	3.38
Synapse	U-Net	Seg-Grad-CAM	0.05	0.431	254.47	0.067
Synapse	U-Net	Seg-Grad-CAM	0.1	0.348	203.74	0.067
Synapse	U-Net	RISE	0.2	0.935	319.11	52
Synapse	U-Net	RISE	0.4	0.656	120.76	52
Synapse	U-Net	MSR	-	0.797	11.43	3.38
Synapse	TransUNet	Seg-Grad-CAM	0.05	0.102	89.36	0.067
Synapse	TransUNet	Seg-Grad-CAM	0.1	0.082	74.86	0.067
Synapse	TransUNet	RISE	0.2	0.92	299.55	52
Synapse	TransUNet	RISE	0.4	0.595	118.08	52
Synapse	TransUNet	MSR	-	0.775	12.61	3.38
COCO-2017	DeepLabv3	Seg-Grad-CAM	0.05	0.693	5.47	0.067
COCO-2017	DeepLabv3	Seg-Grad-CAM	0.1	0.628	4.14	0.067
COCO-2017	DeepLabv3	RISE	0.2	0.883	9.2	52
COCO-2017	DeepLabv3	RISE	0.4	0.639	3.01	52
COCO-2017	DeepLabv3	MSR	-	0.81	0.22	3.38

Table 1: Comparison between Minimally Sufficient Region’s Approach vs. RISE vs. Seg-Grad-CAM on subsets of the Triangle dataset, Synapse dataset, and COCO-2017 dataset. For MSR, the learning rate was kept at 0.1, and λ was kept at 0.01. For RISE, 2000 masks were used. For Seg-Grad-CAM, the layer of application was the bottleneck layer (the ASPP layer for the DeepLabv3 model). The total number of samples was 150, 400, and 181 for Triangle, Synapse, and COCO-2017 datasets respectively. For Dice explained, perturbation ratio, and the time, the mean value has been reported. The best results are reported in bold.

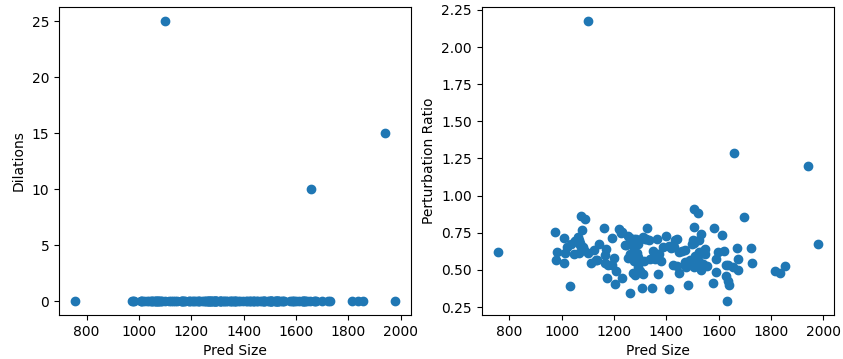


Figure 6: Impact of Prediction Size on a subset of the Triangle dataset. Plot of the No. of Dilations against the Prediction size (left), and the Perturbation Ratio against the Prediction size (right).

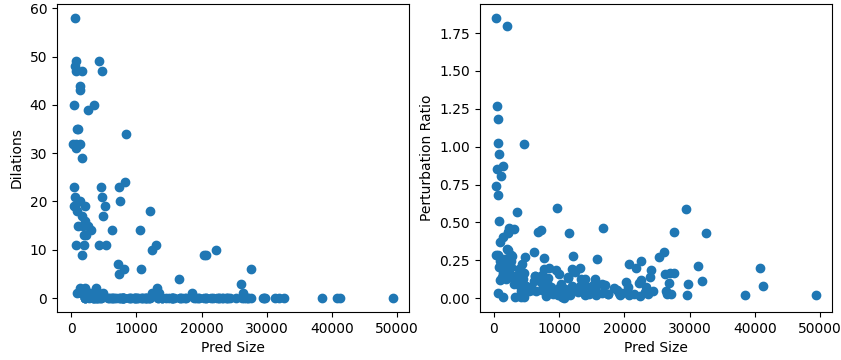


Figure 7: Impact of Prediction Size on a subset of the COCO-2017 dataset. Plot of the No. of Dilations against the Prediction size (left), and the Perturbation Ratio against the Prediction size (right). Results from all eight categories are merged to achieve a single plot.

Dice Explained				Perturbation Ratio			
learning rate				learning rate			
λ	0.001	0.01	0.1	λ	0.001	0.01	0.1
0.001	0.987	0.977	0.969	0.001	0.961	0.96	0.927
0.01	0.987	0.976	0.965	0.01	0.961	0.96	0.627
0.1	0.987	0.976	0.924	0.1	0.961	0.957	0.232

Table 2: Impact of learning rate and λ on a subset of the Triangle Dataset. The mask size was kept at 224×224 . The total number of samples was 150. The left table reports the average Dice explained whereas the right table reports the average perturbation ratio. The best results are reported in bold.

immediately obvious that learning rate and λ are significant parameters for our saliency generation method. The best results are attributable to a learning rate of 0.1 (rightmost column) in each table. For this learning rate, λ of 0.1 returns the best results for **perturbation ratio**, but it seems that it does so at the expense of **Dice explained**. Between 0.001 and 0.01, a λ of 0.01 consistently provides the best balance between our two metrics.

5.4.2 Impact of Mask Size

We report results for 3 mask sizes ranging from 56×56 , 112×112 , and 224×224 . Results for the Triangle, Synapse, and COCO-2017 datasets are displayed in Table. 6. Once again it is clear that mask size is an important parameter,

Dice Explained				Perturbation Ratio			
learning rate				learning rate			
λ	0.001	0.01	0.1	λ	0.001	0.01	0.1
0.001	0.771	0.773	0.794	0.001	140.123	109.974	14.045
0.01	0.768	0.774	0.797	0.01	140.123	97.405	11.431
0.1	0.749	0.78	0.74	0.1	140.123	53.767	5.403

Table 3: Comparison between impact of learning rate and λ on a subset of the Synapse multi-organ CT Dataset. The mask size was kept at 224×224 . The total number of samples was 400 (50 samples per class). The left table reports the average Dice explained whereas the right table reports the average perturbation ratio. The best results are reported in bold.

Dice Explained				Perturbation Ratio			
learning rate				learning rate			
λ	0.001	0.01	0.1	λ	0.001	0.01	0.1
0.001	0.79	0.796	0.767	0.001	158.849	117.877	14.861
0.01	0.788	0.796	0.75	0.01	158.849	104.78	12.742
0.1	0.773	0.783	0.68	0.1	158.849	56.32	4.571

Table 4: Comparison between impact of learning rate and λ on a subset of the Synapse multi-organ CT Dataset. The mask size was kept at 224×224 . The total number of samples was 400 (50 samples per class). The left table reports the average Dice explained whereas the right table reports the average perturbation ratio. The best results are reported in bold.

Dice Explained				Perturbation Ratio			
learning rate				learning rate			
λ	0.001	0.01	0.1	λ	0.001	0.01	0.1
0.001	0.583	0.737	0.824	0.001	3.478	2,749	0.33
0.01	0.583	0.739	0.81	0.01	3.478	2.57	0.215
0.1	0.575	0.736	0.751	0.1	3.478	1.065	0.061

Table 5: Comparison between impact of learning rate and λ on a subset of the COCO-2017 Dataset. The mask size was kept at 224×224 . The total number of samples was 181. The left table reports the average Dice explained whereas the right table reports the average perturbation ratio. The best results are reported in bold.

more so in the domain of **perturbation ratio** as compared to **Dice explained**. Overall, our best results are obtained with a mask size of 224×224 .

5.5 Post-Hoc Assessment of Segmentation Model Reliability

Where saliency maps are a useful and informative tool for the end user, a potentially useful line of study is to identify whether these saliency maps can, in one way or another, be related to the segmentation model’s actual performance. A possible example of this can be a case where saliency maps generated for incorrect model predictions and those

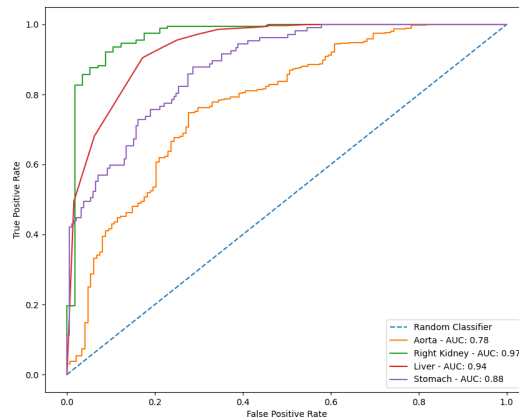


Figure 8: ROC curves of post-hoc reliability classifiers trained for the 'Aorta', 'Right Kidney', 'Liver', and 'Stomach' categories respectively.

Dataset	Model	Mask Size	Dice Explained	Perturbation Ratio
Triangle	U-Net	56	0.975	2.212
Triangle	U-Net	112	0.971	1.56
Triangle	U-Net	224	0.965	0.627
Synapse	U-Net	56	0.769	68.078
Synapse	U-Net	112	0.783	49.478
Synapse	U-Net	224	0.797	11.431
Synapse	TransUNet	56	0.674	67.807
Synapse	TransUNet	112	0.729	52.442
Synapse	TransUNet	224	0.75	12.742
COCO-2017	DeepLabv3	56	0.77	1.97
COCO-2017	DeepLabv3	112	0.808	1.576
COCO-2017	DeepLabv3	224	0.81	0.215

Table 6: Comparison between impact of mask sizes on subsets of the Triangle dataset, Synapse dataset, and COCO-2017 dataset. The learning rate was kept at 0.1, and the λ was kept at 0.01. The total number of samples was 150, 400, and 181 for Triangle, Synapse, and COCO-2017 datasets respectively. For both the Dice explained as well as the perturbation ratio, the mean value has been reported. The best results are reported in bold

Class	No. of Samples	Post-hoc Accuracy	Post-hoc AUC
Aorta	540	0.78	0.78
Gall Bladder	147	0.91	0.95
Left Kidney	242	0.95	0.98
Right Kidney	260	0.93	0.97
Liver	422	0.93	0.94
Pancreas	217	0.98	0.72
Spleen	255	0.78	0.88
Stomach	292	0.77	0.88

Table 7: Post-hoc Model reliability results on eight classes from the Synapse multi-organ dataset

generated for correct model predictions follow different patterns. If this ends up being the case, a discriminative classifier can be trained using saliency maps as features which can act as a proxy for post-hoc model reliability. For any new image, the model’s prediction as well as the saliency map generated for that prediction can be fed into the discriminative classifier from which one could get a certain confidence as to whether this prediction can be considered correct or not.

We utilize three features from our saliency generation process namely (i) the number of dilations required to generate X_{SR} , (ii) the Dice score between the model’s prediction on the original image and the model’s prediction on the minimally sufficient region, and (iii) the ratio of the number of non-zero pixels in the minimally sufficient region to the number of non-zero pixels in the model’s prediction of the object of interest. Given that we already have access to the ground truth Dice values, we train a logistic regression classifier to predict whether the model’s prediction as compared with the ground truth would cross a Dice threshold of 0.9. Results for individual categories can be seen in Table. 7 whereas the ROC curves for a subset of these categories can be seen in Figure. 8.

Unlike image classification where the prediction is binary (either it belongs to the category or it does not), image segmentation is a task involving dense prediction where a meaningful overlap between the ground truth and the segmentation model’s prediction is entirely subjective. It is possible that an overlap of 0.5 is useful enough in certain medical settings, and an overlap of anything less than 0.9 unworthy of consideration in high precision industrialized settings. If saliency maps show the potential to offer assistance in such situations as proxy indicators of the model’s performance in the real world, they can act as an additionally informative feature for the end users, and for certain cases

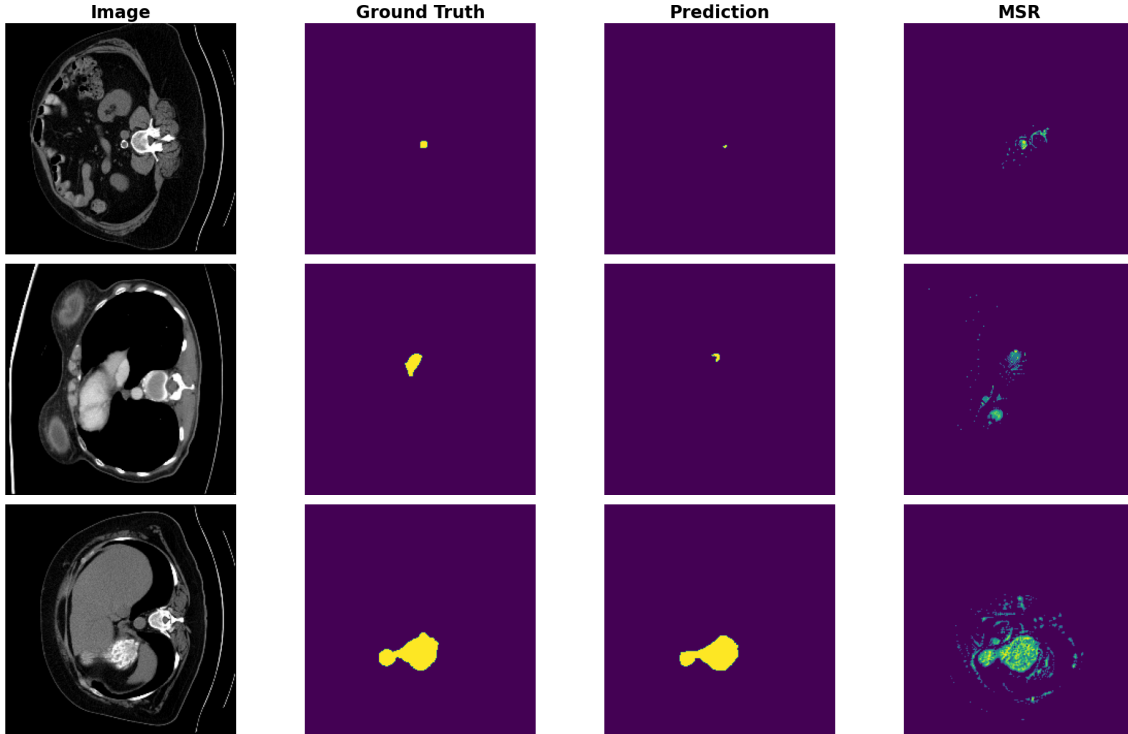


Figure 9: Application of the post-hoc reliability classifier (a simple logistic regression model) on three examples from the Synapse dataset. From top to bottom, the categories are 'Aorta', 'Liver', and 'Stomach'. The post-hoc reliability classifier is correctly able to identify incorrect predictions from the segmentation model for the first and second row as well as the correct prediction from the segmentation model in the third row.

might even offer the potential of automating the pipeline with regards to which of the model's predictions to accept and which one's to reject.

Figure 9 shows three examples to demonstrate the efficacy of our technique. In the first row, the Dice between the aorta as predicted by the segmentation model and the ground truth is clearly less than 0.9. Our post-hoc classifier correctly identifies this with a probability of 0.71. In the second row, once again, the Dice between the liver as predicted by the segmentation model and the ground truth is less than 0.9 and our post-hoc classifier is able to identify this with a probability of 0.72. In the third row, the Dice between the stomach as predicted by the segmentation model and the ground truth is above 0.9, and our post-hoc classifier is able to identify this with a probability of 0.92. Given the absence of ground truth during test time, such a post-hoc classifier can increase the practitioner's trust on the segmentation model's predictions.

5.6 Comparison

The proposed method offers multiple advantages over other existing methods. If we compare it with Seg-Grad-CAM, the minimally sufficient region's approach is model-agnostic whereas Grad-CAM does not fare well for transformer based models due to its explicit reliance on receptive field. Additionally, for Seg-Grad-CAM, the choice of the model's layer is not straightforward, and even though most users apply it to the bottleneck layer of the segmentation model, it is not immediately clear as to why the other layers of the decoder are being ignored. RISE, on the other hand, is a model-agnostic method as well, but it comes with a cumbersome computational cost due to the number of masks it requires to be generated which leads to it working on the order of minutes on a single image whereas the minimally sufficient region's method works on the order of seconds. Also, RISE gives us coarse explanations whereas the proposed method gives us both coarse grained (sufficient region) and fine grained explanations (minimally sufficient regions).

5.7 Limitations

As the method is based on optimization, it naturally involves determining a number of hyperparameters such as λ , α_0 , α_l , learning rate, mask size, and the number of iterations. The most important of these are λ and learning rate as high values for both threaten to destroy the mask entirely whereas low values would make it appear as if no pruning has been done to the mask at all. Additionally, mask size is another important hyperparameter with bigger masks ending up being more pruned as compared to their smaller counterparts. Multiple experiments had to be performed in order to determine these hyperparameters. Also, as the algorithm is based on a perturbation based strategy, it is iterative in nature making it relatively slow as compared to some of the other explainability algorithms such as Seg-Grad-CAM which only require a single forward and backward pass.

6 Conclusion

This work proposes a simple, two stage, model agnostic method, MiSuRe (**M**inimally **S**ufficient **R**egion), to generate saliency maps for image segmentation. The first step, motivated by the inherent bias in image segmentation, is to dilate a mask focusing on the object of interest in order to identify a sufficient region X_{SR} . This sufficient region then serves as the initialization of an optimization process in which the goal is to further prune it in order to arrive at the minimally sufficient region (X_{MSR}). While the sufficient region can be considered as a coarser explanation, the minimally sufficient region provides us with a finer one. This approach can be utilized to extract insights from the segmentation process as a whole, an example of which is to plot the relative size of the visual content required by the segmentation model against the size of the object to be segmented. For the examples considered, this plot reveals an inverse relationship between the two. Additionally, a potential application for this approach is to utilize features obtained from saliency maps in order to train discriminative classifiers which would act as a proxy for the model's predictions on unseen future data. Compared to some of the existing methods of generating saliency maps for image segmentation, the current approach stands-out as being model agnostic, computationally feasible, and providing the end user with a coarse as well as a fine explanation.

References

- Alex Krizhevsky, Ilya Sutskever, and Geoffrey E Hinton. Imagenet classification with deep convolutional neural networks. In NIPS, 2012.
- Karen Simonyan, Andrea Vedaldi, and Andrew Zisserman. Deep inside convolutional networks: Visualising image classification models and saliency maps. In Workshop at International Conference on Learning Representations, 2014.
- Daniel Smilkov, Nikhil Thorat, Been Kim, Fernanda Viégas, and Martin Wattenberg. Smoothgrad: removing noise by adding noise. In ICML Workshop on Visualization for Deep Learning, 2017.
- Mukund Sundararajan, Ankur Taly, and Qiqi Yan. Axiomatic attribution for deep networks. In ICML, 2017.
- Ramprasaath R. Selvaraju, Michael Cogswell, Abhishek Das, Ramakrishna Vedantam, Devi Parikh, and Dhruv Batra. Grad-cam: Visual explanations from deep networks via gradient-based localization. IJCV, 2019.
- Matthew D Zeiler and Rob Fergus. Visualizing and understanding convolutional networks. In ECCV, 2014.
- Marco Tulio Ribeiro, Sameer Singh, and Carlos Guestrin. "why should i trust you?": Explaining the predictions of any classifier. In ACM SIGKDD, 2016.
- Scott Lundberg and Su-In Lee. A unified approach to interpreting model predictions. In NIPS, 2017.
- Vitali Petsiuk, Abir Das, and Kate Saenko. Rise: Randomized input sampling for explanation of black-box models. In BMVC, 2018.
- Maximilian Dreyer, Reduan Achtibat, Thomas Wiegand, Wojciech Samek, and Sebastian Lapuschkin. Revealing hidden context bias in segmentation and object detection through concept-specific explanations. 2023 IEEE/CVF Conference on Computer Vision and Pattern Recognition Workshops (CVPRW), 2023.
- R. Ramprasaath Selvaraju, Michael Cogswell, Abhishek Das, Ramakrishna Vedantam, Devi Parikh, and Dhruv Batra. Grad-cam: Visual explanations from deep networks via gradient-based localization. International Journal of Computer Vision, pages 336–359, 2020. doi:10.1109/ICCV.2017.74.
- Pierre Dardouillet, Alexandre Benoit, Emna Amri, Philippe Bolon, Dominique Dubucq, and Anthony Crédoz. Explainability of image semantic segmentation through shap values. In ICPR Workshop on Explainable and Ethical AI, 2022.

- Kira Vinogradova, Alexandr Dibrov, and Gene Myers. Towards interpretable semantic segmentation via gradient-weighted class activation mapping (student abstract). In AAAI, 2020.
- Bolei Zhou, Aditya Khosla, Agata Lapedriza, Aude Oliva, and Antonio Torralba. Learning deep features for discriminative localization. In CVPR, 2016.
- Jieneng Chen, Yongyi Lu, Qihang Yu, Xiangde Luo, Ehsan Adeli, Yan Wang, Le Lu, Alan L. Yuille, and Yuyin Zhou. Transunet: Transformers make strong encoders for medical image segmentation. In arxiv preprint, arXiv:2102.04306, 2021.
- Ali Hatamizadeh, Yucheng Tang, Vishwesh Nath, Dong Yang, Andriy Myronenko, Bennett Landman, Holger Roth, and Daguang Xu. Unetr: Transformers for 3d medical image segmentation. In WACV, 2022.
- Ruth C. Fong and Andrea Vedaldi. Interpretable explanations of black boxes by meaningful perturbation. 2017 IEEE International Conference on Computer Vision (ICCV), pages 3449–3457, 2017. doi:10.1109/ICCV.2017.371.
- P. Howlader A. Chattopadhyay, A. Sarkar and V. N. Balasubramanian. Grad-cam++: Generalized gradient-based visual explanations for deep convolutional networks. 2018 IEEE Winter Conference on Applications of Computer Vision (WACV), 2018.
- P. T. Jiang, Q. Hou C. B. Zhang, M. M. Cheng, and Y. Wei. Layercam: Exploring hierarchical class activation maps for localization. IEEE Transactions on Image Processing, 2021.
- Haofan Wang, Zifan Wang, Mengnan Du, Fan Yang, Zijian Zhang, Sirui Ding, Piotr Mardziel, and Xia Hu. Score-cam: Score-weighted visual explanations for convolutional neural networks. 2020 IEEE/CVF Conference on Computer Vision and Pattern Recognition Workshops (CVPRW), 2020.
- Saurabh Desai and G. Harish Ramaswamy. Ablation-cam: Visual explanations for deep convolutional network via gradient-free localization. 2020 IEEE Winter Conference on Applications of Computer Vision (WACV), pages 972–980, 2020. doi:10.1109/WACV45572.2020.9093360.
- Sean Mullan and Milan Sonka. Visual attribution for deep learning segmentation in medical imaging. In Medical Imaging 2022: Image Processing, 2022.
- Alvin Wan, Daniel Ho, Younjin Song, Henk Tillman, Sarah Adel Bargal, and Joseph E Gonzalez. Segnbd: Visual decision rules for segmentation. arXiv preprint arXiv:2006.06868, 2020.
- Syed Nouman Hasany, Caroline Petitjean, and Fabrice Mériaudeau. Seg-xres-cam: Explaining spatially local regions in image segmentation. Proceedings of the IEEE/CVF Conference on Computer Vision and Pattern Recognition (CVPR) Workshops, 2023.
- Rokas Gipiškis and Olga Kurasova. Occlusion-based approach for interpretable semantic segmentation. 2023 18th Iberian Conference on Information Systems and Technologies (CISTI), pages 1–6, 2023. doi:10.23919/CISTI58278.2023.10212017.
- Lukas Hoyer, Mauricio Munoz, Prateek Katiyar, Anna Khoreva, and Volker Fischer. Grid saliency for context explanations of semantic segmentation. In NeurIPS, 2019.
- A. Janik, K. Sankaran, and A. Ortiz. Interpreting black-box semantic segmentation models in remote sensing applications. MLVis: Machine Learning Methods in Visualisation for Big Data (2019), 2019.
- Teddy Koker, Fatemehsadat Mireshghallah, Tom Titcombe, and Georgios Kaissis. U-noise: Learnable noise masks for interpretable image segmentation. In 2021 IEEE International Conference on Image Processing (ICIP). IEEE, sep 2021.
- Mateus Riva, Pietro Gori, Florian Yger, and Isabelle Bloch. Is the u-net directional-relationship aware? 2022 IEEE International Conference on Image Processing (ICIP), 2022.
- Bennett Landman, Zhoubing Xu, J Igelsias, Martin Styner, T Langerak, and Arno Klein. Miccai multi-atlas labeling beyond the cranial vault—workshop and challenge. MICCAI Workshop Challenge on Multi-Atlas Labeling Beyond Cranial Vault, 2015.
- Olaf Ronneberger, Philipp Fischer, and Thomas Brox. U-net: Convolutional networks for biomedical image segmentation. In MICCAI, 2015.
- Tsung-Yi Lin, Michael Maire, Serge Belongie, Lubomir Bourdev, Ross Girshick, James Hays, Pietro Perona, Deva Ramanan, C. Lawrence Zitnick, and Piotr Dollár. Microsoft coco: Common objects in context. ECCV, 2014.
- Liang-Chieh Chen, George Papandreou, Florian Schroff, and Hartwig Adam. Rethinking atrous convolution for semantic image segmentation. In arxiv preprint, arXiv:1706.05587, 2017.
- Nicholas Konz, Hanxu Gu, Haoyu Dong, and Maciej A Mazurowski. The intrinsic manifolds of radiological images and their role in deep learning. In International Conference on Medical Image Computing and Computer-Assisted Intervention, pages 684–694. Springer, 2022.